HYDRODYNAMIC CHARACTERISTICS OF HARMONICALLY EXCITED THIN-FILM FLOWS: EXPERIMENTS AND COMPUTATIONS

Charogiannis A.[1], Pradas, M.[1], Denner F.[2], van Wachem B.G.M.[2], Kalliadasis S.[1] and Markides C.N.[1]*
*Author for correspondence
[1]Department of Chemical Engineering, [2]Department of Mechanical Engineering
Imperial College London,
London, SW7 2AZ,
United Kingdom,
E-mail: c.markides@imperial.ac.uk

ABSTRACT

We present new results from the simultaneous application of Planar Laser-Induced Fluorescence (PLIF) and Particle Tracking Velocimetry (PTV), complemented by Direct Numerical Simulations (DNSs), aimed at the detailed hydrodynamic characterization of harmonically excited liquid-film flows. The experimental campaign spans the Reynolds number range $Re = 8 - 320$, and three Kapitza numbers $Ka = 85$, 350 and 1800. PLIF was employed in order to generate spatiotemporally resolved film-height data, and PTV to generate two-dimensional (2D) planar velocity-vector maps of the flow-field underneath the wavy interface. By combining the two optical techniques, instantaneous and highly localised flow-rate data were retrieved, based on which the effect of local film topology on the flow-field is studied in detail. Surprisingly, the instantaneous flow rate is found to vary linearly with the instantaneous film-height, while both experimental and numerical flow-rate data are closely approximated by a simple analytical relationship with only minor deviations. This relationship, which is reported here for the first time, includes the wave speed c and mean flow-rate $\overline{Q}$, both of which can be obtained by simple and inexpensive methods, thus allowing for spatiotemporally resolved flow-rate predictions to be made without requiring any knowledge of flow-field information.

INTRODUCTION

We undertake a combined experimental-computational study dedicated to the detailed hydrodynamic characterisation of isothermal, harmonically excited, gravity-driven liquid films flowing over a flat, inclined plate. Such films are employed in a broad range of industrial applications, such as condensers, evaporators, heat exchangers, and micro-cooling schemes, to name but a few, owing to their high surface-to-volume ratios and excellent heat and mass transfer capabilities even at low liquid-flow rates. It therefore comes as no surprise, that numerous theoretical [1,2], experimental [3,4] and computational [5,6] studies have sought to elucidate the complex flow phenomena underlying these flows, ever since the groundbreaking work of P.L. Kapitza was first published back the late 40s [7].

Despite the numerous experimental studies conducted so far, only a limited number of publications relating to spatiotemporally-resolved variations of the film height and velocity is available, owing to the challenges inherent to the particular measurements. Nevertheless, the application of advanced optical diagnostic techniques, such as Chromatic Confocal Imaging (CCI), PLIF, Particle Image Velocimetry (PIV) and PTV, has contributed significant advancements in our understanding of the physical mechanisms underlying these flows. For example, Dietze and co-workers [8,9] confirmed, the presence of backflow in falling liquid-films using CCI and micro-PIV, Adomeit and Renz [10] and Moran *et. al.* [11] observed systematic deviations from Nusselt velocity-profile predictions depending on film topology using micro-PIV, and Zadrazil and Markides [12] observed multiple recirculation zones within disturbance waves in downwards annular flows by employment of PLIF and PIV.

Despite such novel insights, a systematic study linking spa-

NOMENCLATURE

c	[m s^{-1}]	Wave speed
D	[m]	Characteristic dimension for the Re defintion
f	[s^{-1}]	Forcing/wave frequency
g	[m s^{-2}]	Gravitational acceleration
h	[m]	Film height
Ka	[-]	Kapitza number
Q	[m^3 s^{-1}]	Liquid flow rate
Re	[-]	Reynolds number
t	[s]	Time
u	[m s^{-1}]	Flow velocity
v	[m^2 s^{-1}]	Kinematic viscosity
x	[m]	Distance along the film
y	[m]	Distance across the film

Special characters

β	[°]	Film inclination angle
ρ	[kg m^{-3}]	Density
σ	[N m^{-1}]	Surface tension

Subscripts

f	Fluid
N	Nusselt: Referring to the Nusselt solution
w	Wave
x	Axial direction of the flow

tiotemporally resolved film-height variations to spatiotemporally resolved flow-rate variations in thin liquid-film flows is still lacking. The main purpose of the present paper is to meet this objective by bringing together, for the first time, film-height measurements recovered using PLIF simultaneously with space- and time-resolved velocity measurements generated by application of PTV, as well as high-fidelity numerical results generated via a DNS of the full two-phase system based on a state-of-the-art finite volume method Volume-of-Fluid (VOF) framework.

In our experiments we utilise three Ka number liquids (aqueous glycerol solutions), Re spanning the range $Re = 8 - 320$, and two inlet forcing frequencies, $f_w = 7$ and 10 Hz. The definitions of Re and Ka are given in Equations 1 and 2. Ka represents the dimensionless ratio of surface tension to inertial forces, and acts as an indicator of the hydrodynamic wave regime. Aqueous-glycerol solutions were utilised in order to allow for a wide range of Ka values to be selected. Laminar, as opposed to turbulent falling-films, were investigated in order to allow for direct film-height and flow-field comparisons to DNS and low-dimensional modelling results.

$$Re = \frac{UD}{\nu_f} \tag{1}$$

$$Ka = \frac{\sigma_f}{\rho_f \nu_f^{4/3} (g \sin\beta)^{1/3}} \tag{2}$$

EXPERIMENTAL METHODOLOGY

A detailed description of the experimental setup and data processing methodologies employed in this study can be found elsewhere [13,14], and thus, only a brief synopsis is provided here for completion. The liquid circulates within a closed loop comprising a 400×285 mm glass test-section over which film flows develop. The test section is inclined at $\beta = 20\,^\circ$ to the horizontal, while a settling chamber is installed at the inlet in order to dispense the flow uniformly over the plate. Upstream of the chamber, the flow is split into a steady (Q) and a pulsating supply (Q'), the latter generated using a rotating valve. This arrangement allows for accurate control of both wave frequency and amplitude. The flow rate is measured using an ultrasonic flowmeter which is installed upstream of the settling chamber.

Excitation of the dye- (Rhodamine B) and particle- (glass hollow spheres) seeded flow is performed from the wall side using a double-cavity frequency-doubled Nd:YAG laser (100 Hz). Imaging is also carried out from the same side in order to limit image distortions (see Figure 1). The imaging setup comprises a pair of LaVision CMOS cameras, synchronised with the laser by a LaVision high-speed controller. The imaging planes of the two cameras are mapped and corrected for perspective distortions using a calibration graticule immersed inside the liquid solution, and a pinhole model available in LaVision Davis. The resolution

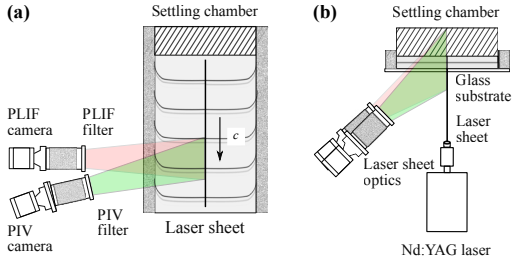

Figure 1: Schematic of the test section showing the orientation of the two cameras and laser relative to illuminated flow domain from: (a) top, and (b) front. Reproduced from reference [13].

varies between 28.0 and 29.7 μm/pixel, and the imaging domain along the film extends to approximately 33 mm.

Sample PLIF and particle images subjected to perspective-distortion corrections and reflection removal are presented in Figure 2. The particle images are used to generate 2-D velocity vector maps PIV calculation) by means of a four-pass cross-correlation approach, with the resulting vector-to-vector spatial resolution varying between $220 - 240$ μm depending on the experimental run. Individual particles are tracked (PTV calculation) by employment of the obtained PIV results as reference estimators of the velocity field.

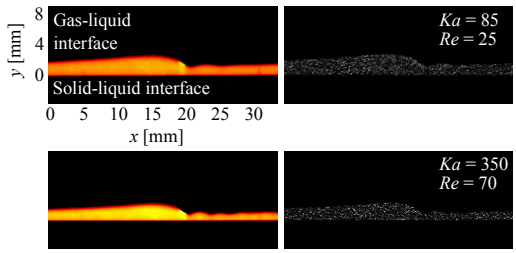

Figure 2: PLIF (left column) and particle (right column) image-pairs, subjected to perspective-distortion corrections and reflection removal. Reproduced from reference [15].

A series of experiments were conducted for error estimation and quality assurance purposes. First, film-height data from flat films ($Ka = 14.1$) were compared to the 1D, steady, fully developed solution of the Navier-Stokes equation under the assumption of negligible inertia (Equation 3), also known as the Nusselt solution [16]. The Nusselt height h_N is expressed as a function of the fluid kinematic viscosity ν_f, the gravitational acceleration g, the inclination angle β and the volumetric flow rate Q. The flow $Re = Q/(\nu_f w) = Q_s/\nu_f$ is expressed as a function of the volumetric flow rate per unit span of the flow, $Q_s = Q/w$, and ν_f. The resulting deviations amount to ≈ 20 μm, with the uncertainty associated with the film-height measurement corresponding to 3%.

$$h_N = \left(\frac{3\nu Q}{g w \sin\beta}\right)^{1/3} = \left(\frac{3\nu^2 Re}{g \sin\beta}\right)^{1/3} \tag{3}$$

Relative deviations were also calculated between PTV-derived

interfacial and bulk velocities on the one hand, and analytical results on the other, with mean values amounting to 3.2% for both test cases. Finally, flow rate comparisons were pursued between LIF/PTV-derived and flowmeter data, with the resulting mean deviation amounting to 1.6% over six flat and nine wavy flows.

DNS METHODOLOGY

DNSs of the entire two-phase system, including the gas and liquid bulk phases ans the gas-liquid interface, are conducted by resolving all relevant length and time scales using a finite-volume framework with collocated variable arrangement [17]. The momentum and continuity equations are solved in a single linear system of equations. The momentum equations are discretized using a second-order backward Euler scheme for the transient term, while spatial terms are discretized using central differencing. The continuity equation is discretized using a balanced-force implementation of the momentum-weighted interpolation method which couples pressure and velocity.

The gas-liquid interface is captured and advected using a compressive (VOF) method [18] and surface tension is described using the CSF model [19]. Gradients in surface tension coefficient as well as mass transfer at the interface are neglected. The volumetric surface force given by the CSF model is discretized on the same computational stencil as the pressure gradient to assure a balanced-force implementation of surface tension [19].

The applied computational domain is chosen to allow a direct comparison with the experimental results and is represented by an equidistant Cartesian mesh with a resolution of 10 cells per equilibrium flat film height. A monochromatic forcing is imposed at the domain inlet by periodically changing the mass flow at a given frequency and amplitude, matching the inlet conditions of the experimental setup.

TRENDS AND RESULTS

Wave characteristics

Examples of typical solitary waves observed in our experiments and simulations are presented in Figure 3. Increasing the flow Re for a fixed Ka results in an increase in the wave-crest height (maximum film-height) as well as the mean film-height. The wave-crest height ceases to increase following the onset of flow recirculation with respect to a frame of reference moving with the wave speed [20]. The wave-trough height (minimum film-height) initially decreases with increasing Re, and then settles to a near-constant value which is independent of the forcing frequency. Consequently, the normalised (by the mean film-height) wave amplitude also increases with increasing Re. Forcing at 7 Hz rather than 10 Hz (for a constant Re) results in a decrease in the number of capillary ripples ahead of the main wave, and an increase in the wave amplitude for $Ka = 85$ and 350 films. In contrast, the $Ka = 1800$ films appear to be unaffected. An excellent agreement between experiments and simulations was obtained for all wave characteristics, such as the mean, maximum and minimum wave-heights, as well as for any flow-field data, including the bulk and interfacial velocities, and

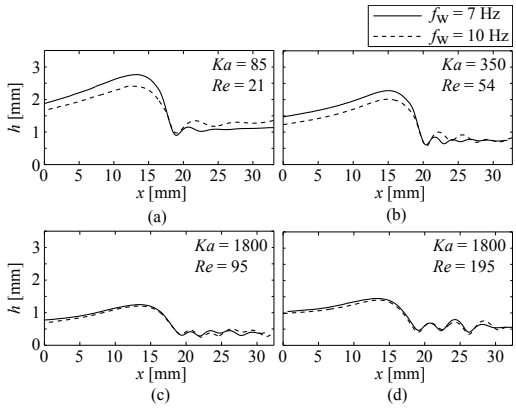

Figure 3: Film height measurements near the crests of solitary waves for two excitation frequencies (7 Hz and 10 Hz) and: (a) $Ka = 85$ and $Re = 21$, (b) $Ka = 350$ and $Re = 54$, (c) $Ka = 1800$ and $Re = 95$ and (d) $Ka = 1800$ and $Re = 195$. Reproduced from reference [15].

axial-velocity profiles. Sample comparisons between film height and interfacial velocity measurements recovered by simultaneous application of PLIF and PTV, and DNSs, are presented in Figure 4.

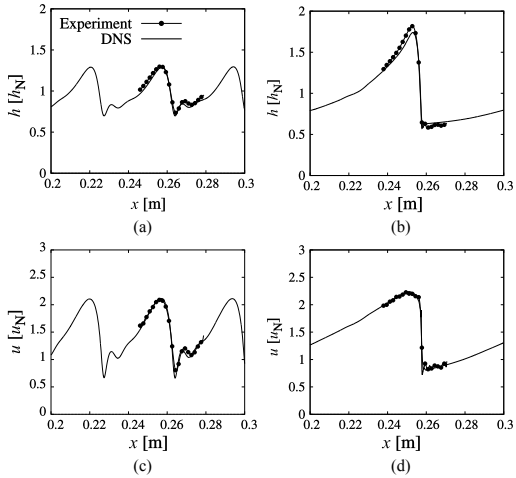

Figure 4: Instantaneous film height h, normalised with the Nusselt height h_N and interface velocity u normalised by the Nusselt velocity u_N, for flows pertaining to $Ka = 85$, $Re = 7.5$ and $f_w = 7$ Hz ((a) and (c)), and $Ka = 350$, $Re = 77$ and $f_w = 7$ Hz ((b) and (d)). Reproduced from reference [20].

Flow rates

Instantaneous and local flow-rate measurements were generated by combining film height and bulk-velocity data. When pursuing flow rate comparisons between waves from different flows, or between experimental results and their analytically derived counterparts, the practice of phase-averaging PTV maps corresponding to the same spatial domain was adopted. This allows us to derive axial velocity profiles at any location along the wave

topology, which when integrated and multiplied by the local film-height and span, yield flow-rate measurements with high spatial resolution. For the same film-height values [16], bulk velocities can be calculated using the corresponding Nusselt relationship, yielding flow-rate predictions. A sample result generated by employment of the particular methodology is presented in Figure 5 (a), revealing pronounced deviations between experiments and analytical results near the wave crest. These can be justified on the following basis: Since the wave-crest height exceeds the mean film-height considerably, any local flow-rate predictions (based on the Nusselt equations) pertain to a film with a constant thickness which exceeds the mean film-thickness. An equivalent

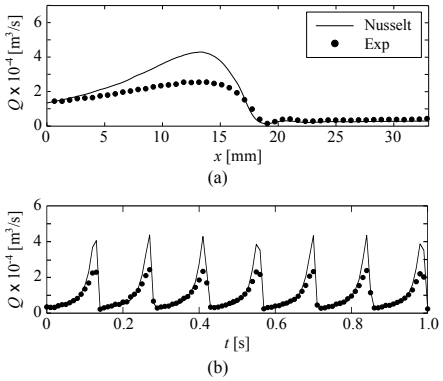

Figure 5: (a) Flow rate comparison of experiments and analytical calculations for a wave pertaining to $Ka = 85$, $Re = 21$ and $f_w = 7$ Hz. (b) Flow rate time-trace generated by simultaneous application of PLF/PTV over a 1-s recording period, for the same flow conditions. Reproduced from reference [15].

analysis was also pursued for time-varying flow rate results, generated using the following approach: Film-height data were averaged over a 1.8 mm region of the flow (along the axial streamwise of the flow) on a per image basis, while averaged axial-velocity profiles were generated over the same spatial domain and integrated over the film height. Thus, every PLIF/PTV image pair contributed a single, local and instantaneous flow-rate measurement. Upon averaging all individual flow rates over an entire image set corresponding to a fixed flow-condition, a mean flow-rate was obtained. A sample flow rate time-trace pertaining to a 1-s recording period is presented in Figure 5 (b), alongside a complementary analytical result.

Correlation between the local and instantaneous film height and flow rate

The flow conditions considered for the purpose of the upcoming analysis span three aqueous-glycerol solutions ($Ka = 85$, 350 and 1800), four Re per liquid composition spanning the ranges Re = 11–25, 37–76 and 94–276, respectively, and two forcing frequencies (f_w = 7 Hz and 10 Hz). DNS data are provided for three Re per liquid solution for flows with $Ka = 85$ and 350.

In an effort to assess the effect of unsteadiness and perform a detailed mass-transfer characterisation, we generated instantaneous flow-rate and film height time-series (see for example Figure 5 (b)), and plotted the results against each other after normalizing by the mean values. Thicker film regions (waves) transport more liquid mass than thinner ones (substrate film), but less than that predicted by the Nusselt solution in the same regions. It should be noted that for a Nusselt flow, a cubic relationship between the flow rate and film height is anticipated, $Q_N \approx h_N^3$.

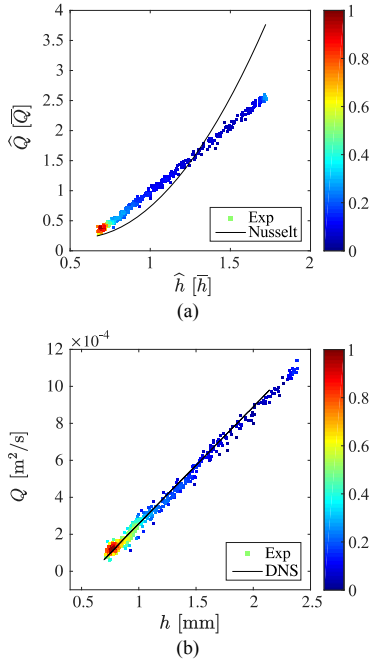

Figure 6: (a) Instantaneous flow-rate data normalised by the mean flow-rate, and plotted against instantaneous film-height data normalised by the mean film-height, for a $Ka = 85$, $Re = 25$ and $f_w = 7$ Hz flow. (b) Instantaneous flow-rates plotted against instantaneous film-heights for a $Ka = 350$, $Re = 65$ and $f_w = 7$ Hz flow from both experimental and DNS data. Reproduced from reference [15].

An example of such a plot is shown in Figure 6 (a), and includes the respective Nusselt predictions of the instantaneous flow-rate based on the measured film heights. The flow-rate data are normalised by the mean flow-rate measured at the downstream location where the flow was imaged, and which is equal by continuity, to the mean flow-rate at the inlet, Q_N, while the film-height data are normalised by the local mean film-height. The colour scheme associated with the data points describes the probability density. It is interesting to note, that based on the experimental data on display, the local and instantaneous flow-rate varies linearly with the local and instantaneous film-height, rather than as $Q \approx h^3$. This is a direct outcome of the deviations between experiments and the Nusselt description observed in Figure 5, and discussed earlier.

Based on similar results generated over the range of examined film-flow conditions, we can report that such linear trends were identified consistently in both experiments and the simula-

tions. Moreover, both the slopes and y-axis intercepts of first-order polynomial fits to the data ($\hat{Q} = A\hat{h} + B$) were found to vary across different flow conditions. In an effort to determine the slopes (A) and intercepts (B) *a priori*, the following analysis was carried out. The continuity equation between two locations along a fully-developed wavy film-flow, x and $x+\delta x$, in a frame of reference moving with the wave speed, c, dictates that:

$$\int_0^{h_{(x)}} (U_{x(x)} - c)\, dy = \int_0^{h_{(x+\delta x)}} (U_{x(x+\delta x)} - c)\, dy, \qquad (4)$$

where $h_{(x)}$ is the film height at x, and $h_{(x+\delta x)}$ the film height at $x+\delta x$. Integrating this equation over the film height, and noting that $h_{(x+\delta x)} = h_x + \delta x$ and $Q_{(x+\delta x)} = Q_x + \delta Q$ results in:

$$\delta Q = c\, \delta x. \qquad (5)$$

Integrating Equation 5 between a location downstream of the inlet where $Q = \overline{Q} = Q_{\mathrm{N}}$ and $h = \overline{h}$, that is, where the local and instantaneous flow-rate and film thickness are equal to the mean flow-rate and mean film-thickness, and any other location farther downstream (x) gives:

$$Q(x) = (\overline{Q} - c\overline{h}) + ch(x), \qquad (6)$$

a relationship that links the local and instantaneous flow-rate per unit span $Q(x)$ to the local and instantaneous film-height $h(x)$, via the wave speed c and the mean flow-rate $\overline{Q}$. The latter also corresponds to the inlet flow-rate Q_{N} (flowmeter measurement), which will be used in the following expressions. A sample plot of the local and instantaneous flow-rate per unit span $Q(x)$ against the local and instantaneous film-height $h(x)$ generated using both experimental and DNS data is provided in Figure 6 (b), for a $Ka = 350$, $Re = 65$ and $f_{\mathrm{w}} = 7$ flow. According to Equation 6, the plotted data should display a first-order polynomial relationship with a slope described by $A = c$ and an intercept $B = \overline{Q} - c\overline{h}$.

Normalizing Equation 6 based on $\overline{Q} = Q_{\mathrm{N}}$ results in the following expression:

$$\frac{Q(x)}{Q_{\mathrm{N}}} = \left(1 - \frac{c\overline{h}}{Q_{\mathrm{N}}}\right) + \frac{c}{Q_{\mathrm{N}}} h(x), \qquad (7)$$

which can be used to describe the data plotted in Figure 6 (a), with $A = c/Q_{\mathrm{N}}$ and $B = 1 - c\overline{h}/Q_{\mathrm{N}}$.

Alternatively, by decomposing $h(x)$ into mean and fluctuating components, $h(x) = \overline{h} + h'(x)$, Equation 6 gives:

$$\frac{Q(x)}{Q_{\mathrm{N}}} = 1 + \frac{c}{Q_{\mathrm{N}}} h(x)', \qquad (8)$$

a first order polynomial expression linking the normalised flow rate $Q(x)/Q_{\mathrm{N}}$ to the film-height fluctuation $h'(x)$, via the coefficients $A = c/Q_{\mathrm{N}}$ and $B = \overline{Q}/Q_{\mathrm{N}} \simeq 1$.

Linear fits were generated for both experimental and numerical data in plots of $h'(x)$ against $Q(x)/Q_{\mathrm{N}}$, and compared to the predictions $A = c/Q_{\mathrm{N}}$ and $B = \overline{Q}/Q_{\mathrm{N}} \simeq 1$. The wave speeds used in the analytically calculated coefficients were obtained directly from the experiments and DNS, while Q_{N}, which is common to both, was measured in the experiments and provided as an input to the DNS scheme. The results for A and B, normalised by their respective analytical values, are presented in Figure 7.

As was noted earlier, Q_{N} is an input to the DNSs and therefore any deviations from $B = 1$ are insignificant ($\leq 1\%$), and probably originate from numerical errors. The experimentally derived values of B, instead, display a mean absolute deviation of 2.5%, which is within the experimental error associated with the flow rate measurement based on the combined PLIF/PTV technique, as well as the error associated with the flowmeter measurement. With respect to the slope results, the deviations amount to 4% and 2% for experiments and DNSs, respectively. Thus, the agreement between experiments, simulations, and the proposed correlation (Equation 8) is excellent.

It is also very interesting to note that the description based on Equation 8 does not require explicit knowledge of the film height, but rather only the fluctuation about some mean value. Consequently, accurate flow-rate data can be determined for any location/instant along the film, even if the real mean film-height is not known; in other words, even if the location of the liquid-solid interface is not identified in the experiment. In fact, from an experimental point of view, the application of this simple linear relationship presupposes knowledge of the mean flow-rate and the wave speed only, while dispensing of a significant error source, the location of the gas-liquid interface. The mean flow-rate can be easily obtained using a flowmeter, whereas the wave speed can be measured by simple direct imaging (without the need for an expensive and complex PLIF-PIV setup).

CONCLUSION

PLIF was used to recover spatiotemporally resolved film-height data, simultaneously with PTV which was employed in order to to retrieve planar velocity-vector maps of the flow-field underneath the wavy interface. By combining the two techniques, instantaneous and highly localised flow-rate data were also recovered, in order to perform a detailed hydrodynamic characterisation of the film flows under investigation. The experimental campaign was complemented by state-of-the-art DNSs. To the best knowledge of the authors, this is the first time that an arsenal of experimental techniques in conjunction with detailed numerical simulations have been applied to free-surface thin-film flows.

The measurement errors associated with the film-height, velocity and flow-rate measurements do not exceed 4%, resulting in an excellent agreement between experiments and simulations. From comparisons of film-height and flow-rate results, and the

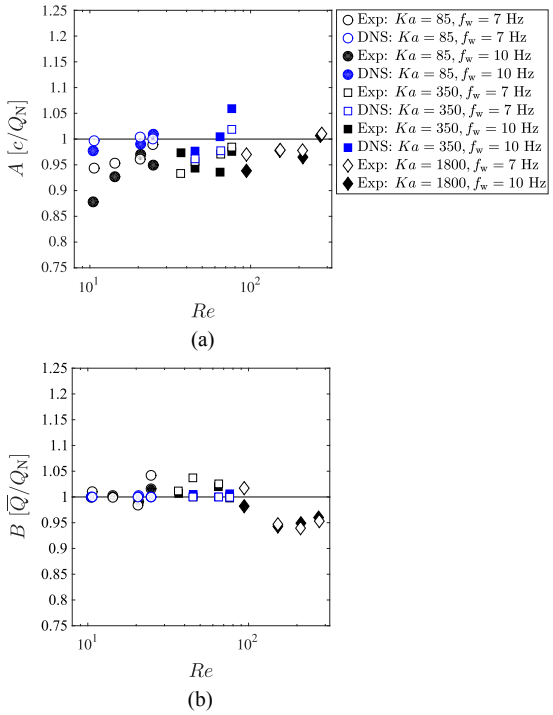

Figure 7: Results for coefficients generated by linear fits to local and instantaneous, normalised flow-rate and film-height fluctuation data. Reproduced from reference [12].

application of continuity between two locations along a fully-developed wavy film-flow in a frame of reference moving with the wave speed, the instantaneous flow-rate was found to vary linearly with the instantaneous film-height. The slopes and y-intercepts of linear fits to the data were closely approximated by a simple analytical relationship with only minor deviations. This previously unavailable correlation includes the wave speed c and mean flow-rate $\overline{Q}$, both of which can be obtained by relatively straightforward and inexpensive methods, thus allowing for spatiotemporally resolved flow-rate predictions to be made without requiring any detailed knowledge of the flow field.

ACKNOWLEDGEMENT

We acknowledge financial support by the UK Engineering and Physical Sciences Research Council (EPSRC) through Grants Nos. EP/K008595/1, EP/L020564/1 and EP/M021556/1.

REFERENCES

[1] Pradas M., Tseluiko D., and Kalliadasis S., Rigorous coherent-structure theory for falling liquid films: Viscous dispersion effects on bound-state formation and self-organization, *Physics of Fluids*, Vol. 23, 2011, pp. 044104-1-19

[2] Goussis D.A., and Kelly R.E., Surface wave and thermocapillary instabilities in a liquid film flow, *Journal of Fluid Mechanics*, Vol. 223, 1991, pp. 2545

[3] Alekseenko S.V., Nakoryakov V.Y., and Pokusaev B.G., Wave formation on a vertical falling liquid film, *AIChE Journal*, Vol. 31, 1985, pp. 14461460

[4] Mathie R., Nakamura H., and Markides C.N., Heat transfer augmentation in unsteady conjugate thermal systems - Part II: Applications, *International Journal of Heat and Mass Transfer*, Vol. 56, 2013, pp. 819-833

[5] Chakraborty S., Nguyen P.-K., Ruyer-Quil C., and Bontozoglou V., Extreme solitary waves on falling liquid films, *Journal of Fluid Mechanics*, Vol. 745, 2014, pp. 564591

[6] Rohlfs W. and Scheid B., Phase diagram for the onset of circulating waves and flow reversal in inclined falling films, *Journal of Fluid Mechanics*, Vol. 763, 2015, pp. 322-352

[7] Kapitza P.L., Wave flow of thin layers of a viscous fluid: I. Free flow, *Zhurnal Eksperimentalnoi I Teoreticheskoi Fiziki*, Vol. 18, 1948, pp. 3-18

[8] Dietze G.F., Al-Sibai F., and Kneer R., Experimental study of flow separation in laminar falling liquid films, *Journal of Fluid Mechanics*, Vol. 637, 2009, pp. 73-104

[9] Dietze G.F., Leefken A., and Kneer R., Investigation of the backflow phenomenon in falling liquid films, *Journal of Fluid Mechanics*, Vol. 595, 2008, pp. 435-459

[10] Adomeit P., and Renz U., Hydrodynamics of three-dimensional waves in laminar falling films, *International Journal of Multiphase Flow*, Vol. 26, 2000, pp. 1183-1208

[11] Moran K., Inumaru J., and Kawaji M., Instantaneous hydrodynamics of a laminar wavy liquid film, *International Journal of Multiphase Flow*, Vol. 28, 2002, pp. 731755.

[12] Zadrazil I., Matar O.K., and Markides C.N., An experimental characterization of liquid films in downwards co-current gas-liquid annular flow by particle image and tracking velocimetry, *International Journal of Multiphase Flow*, Vol. 68, 2014, pp. 1-12

[13] Charogiannis A., An J.S., and Markides C.N., A Simultaneous Laser-Induced Fluorescence, Particle Image Velocimetry and Particle Tracking Velocimetry Technique for the Investigation of Liquid Film Flows, *Experimental Thermal and Fluid Science*, Vol. 68, pp. 516-536

[14] Markides C.N., Mathie R., and Charogiannis A., An experimental study of spatiotemporally resolved heat transfer in thin liquid-film flows falling over an inclined heated foil, *International Journal of Heat and Mass Transfer*. Vol. 93, 2015, pp. 872-888

[15] Charogiannis A., Denner F., van Wachem B.G.M., Kalliadasis S., and Markides C.N., Detailed hydrodynamic characherization of harminically excited falling-film flows: A combined experimental and computational study, *Submitted to Physical Review Fluids*, 2016

[16] Nusselt W., Die Oberflachenkondensation des Wasserdampfes, *Zhurnal Vereines Deutscher Ingenieure*, Vol. 60, 1916, pp. 541-546

[17] Denner F., and van Wachem B.G.M., Fully-coupled balanced-force VOF framework for arbitrary meshes with least-squares curvature evaluation from volume fractions, *Numerical Heat Transfer Part B-Fundamentals*, Vol. 65, 2014, pp. 218-255

[18] Denner F., and van Wachem B.G.M., Compressive VOF method with skewness correction to capture sharp interfaces on arbitrary meshes, *Journal of Computational Physics*, Vol. 279, 2014, pp. 127-144

[19] Brackbill J., Kothe D., and Zemach C., Continuum method for modeling surface tension, *Journal of Computational Physics*, Vol. 100, 1992, pp. 335-354

[20] Denner F., Charogiannis A., Pradas M., van Wachem B.G.M., Markides C.N., and Kalliadasis S., Solitary waves on falling liquid films in the drag-inertia regime: computations and experiments, *Submitted to Journal of Fluid Mechanics*, 2015